Interfacial Effects in Iron-Nickel Hydroxide–Platinum Nanoparticles Enhance Catalytic Oxidation

Guangxu Chen *et al.*

Science **344**, 495 (2014);
DOI: 10.1126/science.1252553

The unexpected homogeneous exchange can be rationalized by the presence of disordered domains inside the ordered hydrogen-bonded supramolecular polymer (*13*, *22*); a more detailed description is provided in the supplementary materials (*12*). In the disordered domains the interactions between monomers are proposed to be weaker and, hence, allow an easy point for monomers to leave and enter the 1D fiber. The observed exchange rate is relatively slow compared with the dynamics of the internal order within the fiber. Therefore, within the spatial and temporal resolution of the STORM technique [down to 50 nm (fig. S14)], which corresponds to ~10 times the fiber diameter, the BTA-based supramolecular polymers presented here exchanged homogenously along the polymer backbone. No evidence is obtained for any fragmentation-fusion or polymerization-depolymerization at the chain ends. This finding suggests the need to revisit the dynamic behavior of many other supramolecular fibers (*3*).

References and Notes

1. D. A. Fletcher, R. D. Mullins, *Nature* **463**, 485–492 (2010).
2. F. Chiti, C. M. Dobson, *Annu. Rev. Biochem.* **75**, 333–366 (2006).
3. T. Aida, E. W. Meijer, S. I. Stupp, *Science* **335**, 813–817 (2012).
4. T. P. J. Knowles *et al*., *Science* **326**, 1533–1537 (2009).
5. F. Würthner, T. E. Kaiser, C. R. Saha-Möller, *Angew. Chem. Int. Ed.* **50**, 3376–3410 (2011).
6. D. Zhao, J. S. Moore, *Org. Biomol. Chem.* **1**, 3471–3491 (2003).
7. B. Huang, M. Bates, X. Zhuang, *Annu. Rev. Biochem.* **78**, 993–1016 (2009).
8. A. Szymborska *et al*., *Science* **341**, 655–658 (2013).
9. D. Pinotsi *et al*., *Nano Lett.* **14**, 339–345 (2014).
10. S. Cantekin, T. F. A. de Greef, A. R. A. Palmans, *Chem. Soc. Rev.* **41**, 6125–6137 (2012).
11. L. Albertazzi *et al*., *Proc. Natl. Acad. Sci. U.S.A.* **110**, 12203–12208 (2013).
12. Materials and methods are available as supplementary materials on *Science* Online.
13. C. M. A. Leenders *et al*., *Chem. Commun.* **49**, 1963–1965 (2013).
14. M. J. Rust, M. Bates, X. Zhuang, *Nat. Methods* **3**, 793–796 (2006).
15. P. Sengupta, T. Jovanovic-Talisman, J. Lippincott-Schwartz, *Nat. Protoc.* **8**, 345–354 (2013).
16. X. Nan *et al*., *Proc. Natl. Acad. Sci. U.S.A.* **110**, 18519–18524 (2013).
17. R. P. J. Nieuwenhuizen *et al*., *Nat. Methods* **10**, 557–562 (2013).
18. J. Adamcik *et al*., *Nat. Nanotechnol.* **5**, 423–428 (2010).
19. G. T. Dempsey, J. C. Vaughan, K. H. Chen, M. Bates, X. Zhuang, *Nat. Methods* **8**, 1027–1036 (2011).
20. F. Valle, M. Favre, P. De Los Rios, A. Rosa, G. Dietler, *Phys. Rev. Lett.* **95**, 158105 (2005).
21. S. L. Veatch *et al*., *PLOS ONE* **7**, e31457 (2012).
22. T. Shikata, D. Ogata, K. Hanabusa, *J. Phys. Chem. B* **108**, 508–514 (2004).

Acknowledgments: We thank X. Zhuang and Nikon Europe for sharing data sets. Data sets for in vitro microtubules (*18*) were provided by X. Zhuang; data sets for microtubules in BSC-1 cells were provided by Nikon Europe. We thank T. de Greef and A. Palmans for useful discussions and the Institute for Complex Molecular Systems animation studio for the artwork. This work was supported by the European Research Council; the Dutch Science Foundation (NWO); the Netherlands Initiative for Regenerative Medicine; and the Dutch Ministry of Education, Culture and Science (Gravity program 024.001.035).

Supplementary Materials

www.sciencemag.org/content/344/6183/491/suppl/DC1
Materials and Methods
Supplementary Text
Figs. S1 to S24
References (*23*–*25*)
Appendices S1 to S3

16 January 2014; accepted 7 April 2014
10.1126/science.1250945

Interfacial Effects in Iron-Nickel Hydroxide–Platinum Nanoparticles Enhance Catalytic Oxidation

Guangxu Chen,[1] Yun Zhao,[1] Gang Fu,[1]* Paul N. Duchesne,[3] Lin Gu,[2]* Yanping Zheng,[1] Xuefei Weng,[1] Mingshu Chen,[1] Peng Zhang,[3] Chih-Wen Pao,[4] Jyh-Fu Lee,[4] Nanfeng Zheng[1]*

Hybrid metal nanoparticles can allow separate reaction steps to occur in close proximity at different metal sites and accelerate catalysis. We synthesized iron-nickel hydroxide–platinum (transition metal-OH-Pt) nanoparticles with diameters below 5 nanometers and showed that they are highly efficient for carbon monoxide (CO) oxidation catalysis at room temperature. We characterized the composition and structure of the transition metal–OH-Pt interface and showed that Ni^{2+} plays a key role in stabilizing the interface against dehydration. Density functional theory and isotope-labeling experiments revealed that the OH groups at the Fe^{3+}-OH-Pt interfaces readily react with CO adsorbed nearby to directly yield carbon dioxide (CO_2) and simultaneously produce coordinatively unsaturated Fe sites for O_2 activation. The oxide-supported PtFeNi nanocatalyst rapidly and fully removed CO from humid air without decay in activity for 1 month.

The fabrication of multicomponent active sites (*1*–*15*), particularly metal-metal hydroxide and oxide interfaces (*1*–*11*), to facilitate the activation of reagents has been emerging as an effective method for preparing heterogeneous catalysts with improved activities. For example, Pt/FeO_x interfaces exhibit excellent performance in CO oxidation and CO preferential oxidation (PROX) (*1*, *2*), Au/CeO_x and Au/TiO_x interfaces improve the activity of the water-gas shift reaction (*5*–*7*), and $Pt/M(OH)_2$ (where M is metal) interfaces enhance the performance of H_2 evolution reaction (*10*, *11*). The structure and reactivity of such catalysts can be modeled with well-defined synthetic nanoparticles (NPs) (*16*–*18*). For instance, rational design of nanoscaled metal–metal oxide interfaces in nanostructured catalysts has been successfully achieved by controlled assembly of metal and metal oxide nanocrystals (NCs) (*8*). Monodisperse Pd NCs were deposited on ceria to investigate the $Pd\text{-}CeO_2$ interfacial effect on catalysis (*19*). However, assembling metal NPs with oxide NPs or depositing metal NPs on oxide supports introduced rather limited metal-metal (hydr)oxide interfaces.

We report on a wet-chemical method for fabricating M-OH-Pt interfaces (M-OH, where M is Fe and Ni) by partially covering the surface of monodisperse Pt NCs (which are <5 nm in diameter) with atomically thick M-OH layers. The Fe^{3+}-OH-Pt interfaces increased room-temperature catalytic CO oxidation by generating coordinatively unsaturated iron sites for activating O_2, and the Ni^{2+} incorporation dramatically enhanced the long-term catalyst stability by stabilizing the Fe^{3+}-OH-Pt interfaces during catalysis. Based on this understanding, an alloy-assisted strategy was developed to produce a practical Pt nanocatalyst with catalytic M-OH-Pt sites over 50% of total Pt atoms in the catalyst.

To create the iron (hydr)oxide interface, monodisperse Pt NCs capped by organic amine (fig. S1) were synthesized by thermally reducing $Pt(acac)_2$ (where acac is acetylacetonate) in the presence of CO. A small amount of $Fe(acac)_3$ was then introduced and thermally decomposed to deposit submonolayer $Fe(OH)_x$ onto the surface of the premade Pt NCs, yielding the $Pt/Fe(OH)_x$ composite (*20*). Aberration-corrected scanning transmission electron microscopy (STEM) images (Fig. 1, B and C, and fig. S2) revealed the deposition of a less electron-dense layer on the Pt NCs; energy-dispersive spectroscopy (EDS) analysis showed that this layer contained iron (fig. S3). Although the surface of the Pt NCs was covered by iron

[1]State Key Laboratory for Physical Chemistry of Solid Surfaces, Collaborative Innovation Center of Chemistry for Energy Materials, National Engineering Laboratory for Green Chemical Productions of Alcohols, Ethers, and Esters, and Department of Chemistry, College of Chemistry and Chemical Engineering, Xiamen University, Xiamen 361005, China. [2]Institute of Physics, Chinese Academy of Sciences, Beijing 100190, China. [3]Department of Chemistry, Dalhousie University, Halifax, NS, B3H 4R2, Canada. [4]National Synchrotron Radiation Research Center, Hsinchu 30076, Taiwan.

*Corresponding author. E-mail: nfzheng@xmu.edu.cn (N.F.Z.); l.gu@iphy.ac.cn (L.G.); gfu@xmu.edu.cn (G.F.)

species, lattice fringes with interplanar distances of 0.23 nm, corresponding to Pt(111) planes, were observed. The Fe x-ray photoelectron spectroscopy (XPS) spectra suggested an Fe^{3+} oxidation state (Fig. 1C and fig. S4). The O1s XPS spectra are best fitted by the presence of Fe-OH and bridging oxo groups (*21*) in a 4.2:1 ratio (Fig. 1D). X-ray absorption near-edge structure (XANES) analysis (fig. S5) at the pre-edge of the Fe K-edge at 7.114 keV showed that the Fe-O coordination sphere is a slightly distorted octahedron (*22*). Extended x-ray absorption fine structure (EXAFS) revealed that the bond distances of Fe-O and Fe-Fe in the overgrown $Fe(OH)_x$ layer were 1.97 ± 0.02 Å and 3.01 ± 0.02 Å, respectively (fig. S5 and table S1), and an Fe-O coordination of 6 ± 1. Low-energy ion scattering spectroscopy (LEISS) (fig. S6) showed that the as-obtained $Pt/Fe(OH)_x$ NPs still had open Pt sites at their edges and corners.

Given the strong binding of CO to Pt (*1*), we studied CO oxidation to evaluate the Fe^{3+}-OH-Pt interfacial effect. TiO_2-supported Pt NCs displayed negligible CO oxidation activity at room temperature (Fig. 1E); 100% CO conversion was achieved only at temperatures above 373 K. However, TiO_2-supported $Pt/Fe(OH)_x$ NPs (fig. S7) readily achieved 100% CO conversion at room temperature, even with a space velocity (SV) as high as ~400 L g^{-1} Pt h^{-1} (Fig. 1E). The enhanced activity of $Pt/Fe(OH)_x$ NPs was also observed in a humid stream with less oxidizing reactant (reducing the O_2/CO ratio from 16 to 4) (fig. S8). The activity was lost when the $Pt/Fe(OH)_x$ catalyst was simply treated with nitric acid (fig. S9). A decline in activity from 100 to 27% in 70 min occurred when the reaction was switched from humid air to dry air (fig. S10). Even in a humid reaction stream with a relative humidity of 50%, the $Pt/Fe(OH)_x$ catalyst began to degrade after 8 hours at room temperature. We propose that the activity decrease was caused by instability of the interfacial Fe^{3+}-OH-Pt sites with respect to dehydration. Because CO oxidation is exothermic, we subjected the $Pt/Fe(OH)_x$ catalyst to thermal treatment at 453 K in dry air for 2 hours. The OH:O ratio from the O1s XPS was reduced to only 2.7 (fig. S11), suggesting the loss of water. The $Fe(OH)_x$ submonolayers dehydrated into three-dimensional iron oxide-hydroxide or iron oxide.

To prevent the dehydration-induced loss of Fe^{3+}-OH-Pt sites, Ni^{2+}, which forms a stable, layered structure of $Ni(OH)_2$ with nearly perfect octahedral coordination, was incorporated into the $Fe(OH)_x$ submonolayer. The ready formation of hydrotalcite-like Ni/Fe hydroxides (*23*, *24*) was expected to stabilize catalytically active Fe^{3+}-OH-Pt interfacial sites through the strong interaction between $Ni(OH)_x$ and $Fe(OH)_x$. Moreover, $Ni(OH)_2$ species are active in the dissociation of adsorbed water molecules and in proton transport

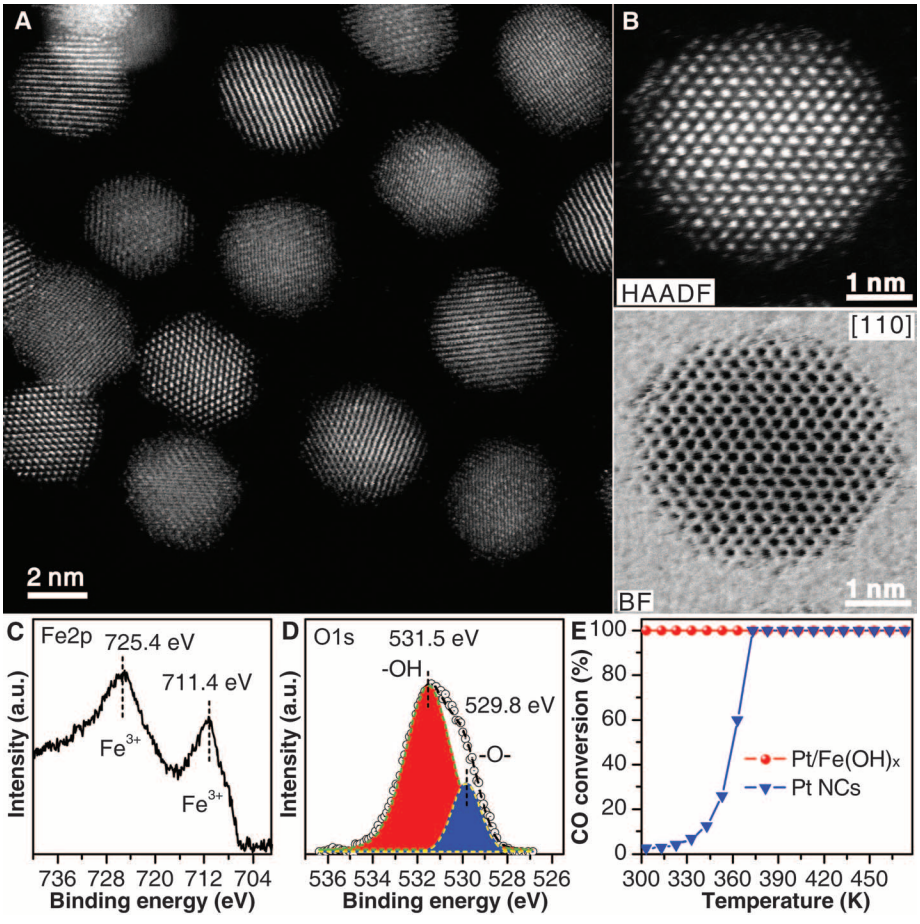

Fig. 1. Structural characterizations and catalytic performance of the $Pt/Fe(OH)_x$ nanoparticles. (**A**) Representative high-angle annular dark-field (HAADF) STEM image of $Pt/Fe(OH)_x$ NPs. (**B**) High-resolution HAADF-STEM image projected along [110] axis and the corresponding bright-field image of an individual $Pt/Fe(OH)_x$ NP. (**C** and **D**) XPS core-level spectra of Fe2p and O1s, respectively. (**E**) CO conversions as a function of reaction temperature over TiO_2-supported $Pt/Fe(OH)_x$ NPs and Pt NCs. Reaction conditions: 1% CO; 16% O_2; N_2 balance; SV = 400 L g^{-1} Pt h^{-1}; pressure = 0.1M Pa.

Fig. 2. Structural characterizations and catalytic performance of the $Pt/FeNi(OH)_x$ nanoparticles. (**A**) Representative HAADF-STEM image of $Pt/FeNi(OH)_x$ NPs. (**B**) STEM-EDS elemental mapping of a single $Pt/FeNi(OH)_x$ NP. (**C**) Catalytic performances of TiO_2-supported $Pt/FeNi(OH)_x$ NPs, Pt NCs, and $Pt/Fe(OH)_x$ NPs as a function of time-on-stream. Reaction conditions: 1% CO; 16% O_2; N_2 balance; T = 303 K; SV = 400 L g^{-1} Pt h^{-1}; relative humidity = 50%; pressure = 0.1M Pa.

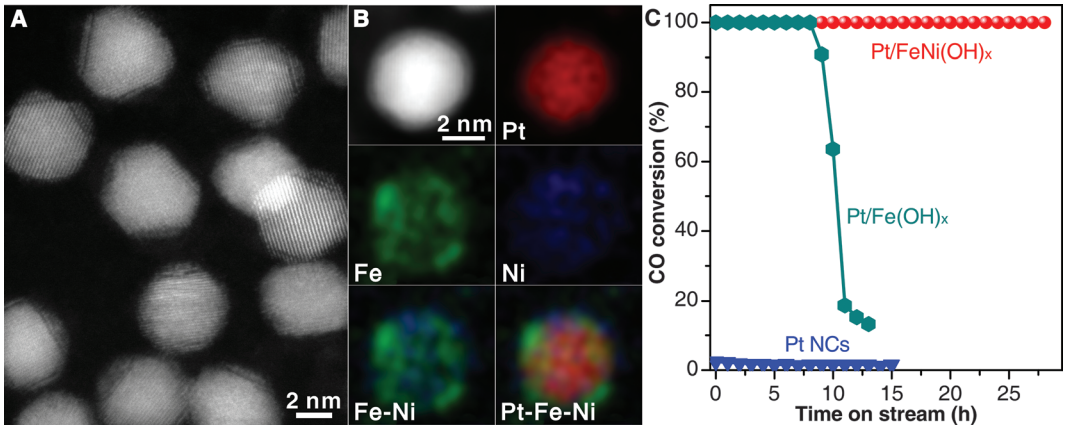

(*11*, *25*). The addition of a $Ni(acac)_2$ precursor during the thermal overgrowth process deposited $FeNi(OH)_x$ hybrid submonolayers on Pt NCs with a boundary gap of 3 Å (Fig. 2A). STEM-EDS measurements showed that the $Fe(OH)_x$ and $Ni(OH)_x$ were mixed on the surface (Fig. 2B). As identified by LEISS (fig. S12), open Pt sites were present with Ni and Fe on the outermost surface of the $Pt/FeNi(OH)_x$ NPs. The XANES and EXAFS analyses of $Pt/FeNi(OH)_x$ (fig. S13) indicated that $Ni(OH)_2$ was present in a nearly perfect octahedral coordination environment with Ni-O distances of 2.05 ± 0.01 Å (table S2), and iron was still present as Fe^{3+}. The O1s XPS spectrum indicated an OH:O ratio of 7.5 (fig. S14A).

The $Pt/FeNi(OH)_x$ NPs exhibited greater stability in CO oxidation. When loaded onto supports (fig. S15), the $Pt/FeNi(OH)_x$ catalyst was stable in the reaction stream for more than 28 hours without any decrease in its activity at room temperature (Fig. 2C) and achieved 100% CO conversion (fig. S16). After a 2-hour heat treatment at 453 K under reaction atmosphere, the OH:O ratio in the $Pt/FeNi(OH)_x$ catalyst was maintained at 5.3 (fig. S14B). In comparison, NPs with $Ni(OH)_x$ submonolayer grown on Pt NCs, denoted as $Pt/Ni(OH)_x$, performed poorly at room temperature relative to $Pt/Fe(OH)_x$ (figs. S17 and S18).

To understand how the Fe^{3+}-OH-Pt interface promoted the activity of the catalysts, structural models of periodic Pt [n(111)×(111)] and [n(111)×(100)] stepped surfaces with the overgrowth of $Fe(OH)_x$ on (111) terraces (figs. S19 to S21 and table S3) were built to simulate the hydroxide overgrowth structures on Pt NCs and optimized by using Vienna Ab-initio Simulation Package (VASP) code. Density functional theory (DFT) calculations suggested that CO oxidation at the interfacial Fe^{3+}-OH-Pt site could be triggered by the coupling reaction between the adsorbed CO and interfacial –OH moieties (Fig. 3A), leading to formation of CO_2 either directly or via –COOH intermediate (figs. S22 to S24) with a low energy barrier of 0.69 eV (or 0.93 eV). On the [n(111)×(111)] stepped surface, the release of CO_2 created a vacancy at the interface (i.e., Fe-Vac-Pt, where Vac is a vacancy) with an activation barrier and reaction energy of 0.16 and –0.66 eV (Fig. 3A), respectively. The proton on the reacted interfacial –OH was transferred to nearby –OH to form adsorbed H_2O. On the interfacial Fe-Vac-Pt site, O_2 adsorption was preferential to CO adsorption (–1.34 versus –0.87 eV) (fig. S21), suggesting that the created interfacial vacancy readily served as an effective adsorption site to convert O_2 into highly reactive –OOH species (table S3). The produced –OOH species readily coupled with the second CO directly to form CO_2, simultaneously recovering the Fe^{3+}-OH-Pt interfaces and completing the catalytic cycle. Such H_2O-mediated proton transfer often occurs on the surface of solid oxides (e.g., iron oxide) (*26*) and in our case facilitates the whole catalytic oxidation process (fig. S10).

The reported mechanisms for CO oxidation over $Pt\text{-}FeO_x$ catalysts begin with O_2 activation, either at coordinatively unsaturated Fe^{2+} sites on Pt (*1*) or at an oxygen vacancy on the hematite surface (*2*). These coordinatively unsaturated O_2 activation sites were mainly generated by thermally prereducing the $Pt\text{-}FeO_x$ catalysts in H_2 and were unstable in air. However, our Fe^{3+}-OH-Pt mechanism suggests that these Fe^{2+} sites are not a prerequisite for CO oxidation and that coordinatively saturated Fe^{3+} species are more stable under ambient conditions. We verified the above mechanism by using isotope-labeling experiments (*20*). In the absence of O_2, 55% of the total CO_2 yielded in the first five pulses was determined by mass spectroscopy to be singly ^{18}O-labeled CO_2 ($C^{16}O^{18}O$) when $C^{16}O$ was pulsed into the $H_2{}^{18}O$ pretreated $Pt/Fe(OH)_x$ catalyst (Fig. 3B). The production of $C^{16}O^{18}O$ declined with the increased number of CO pulses because of the continuous consumption of the interfacial $-{}^{18}OH$ groups. In comparison, the reaction of a $C^{16}O$ pulse with the untreated $Pt/Fe(OH)_x$ catalyst yielded negligible $C^{16}O^{18}O$ (Fig. 3C). While confirming that CO could directly react with the interfacial Fe^{3+}-OH-Pt sites to yield CO_2, this result also suggested that ^{18}O-labeled interfacial Fe^{3+}-^{18}OH-Pt sites were readily obtained by treating the $Pt/Fe(OH)_x$ catalyst with $H_2{}^{18}O$. Thus, it was not surprising that the reaction of pulses containing CO, O_2, and $H_2{}^{18}O$ in N_2 with the $Pt/Fe(OH)_x$ catalyst steadily yielded much more $C^{16}O^{18}O$ than those pulses containing CO, O_2, and non-^{18}O–labeled H_2O (Fig. 3, D and E). In all of our isotope-labeling experiments, no detectable isotope exchange between H_2O and O_2 was observed (fig. S25).

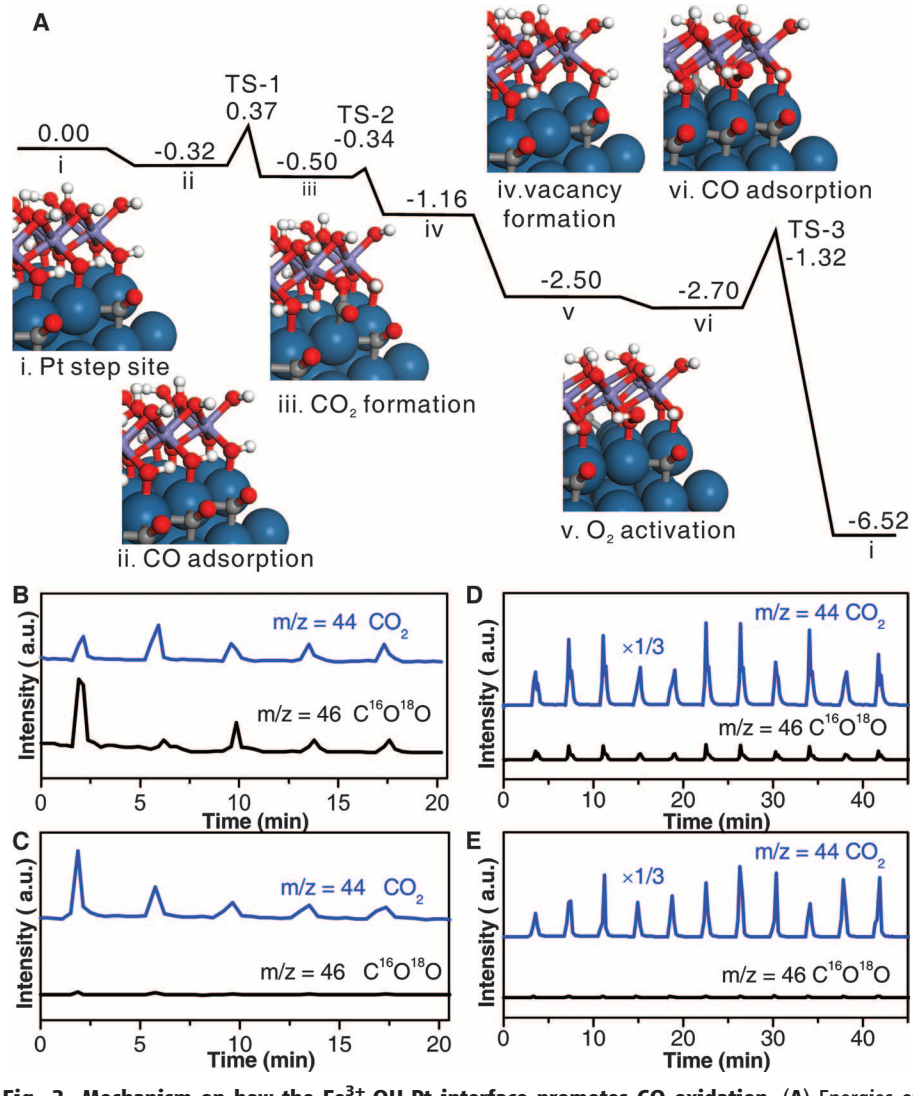

Fig. 3. Mechanism on how the Fe^{3+}-OH-Pt interface promotes CO oxidation. (**A**) Energies of intermediates and transition states in the mechanism of CO oxidation at the Fe^{3+}-OH-Pt[n(111)×(111)] interfaces from DFT calculation. (**B** and **C**) Time-dependent mass spectra of $C^{16}O_2$ and $C^{16}O^{18}O$ species during the pulse experiments by pulsing CO into the $Pt/Fe(OH)_x$ catalyst with (B) and without (C) $H_2{}^{18}O$ pretreatment. (**D** and **E**) Time-dependent mass spectra of $C^{16}O_2$ and $C^{16}O^{18}O$ species during the pulse experiments by reacting the $Pt/Fe(OH)_x$ catalyst with pulses containing a mixture of CO, O_2, and $H_2{}^{18}O$ (D) or normal H_2O (E) in N_2.

Our Fe^{3+}-OH-Pt mechanism was also confirmed by kinetic studies. Over the catalysts incorporated with $Fe(OH)_x$, the activation energies of CO oxidation were reduced to 16 kJ/mol compared with 51 kJ/mol for TiO_2-supported Pt NCs (fig. S26). The incorporation of Ni^{2+} did not reduce the activation energy further. Over TiO_2-supported Pt/$Fe(OH)_x$, the introduction of humidity reduced the activation energy to 12 kJ/mol. Moreover, CO oxidation was determined to be close to zero order for CO and first order for O_2 (fig. S27), which is expected from the Fe^{3+}-OH-Pt mechanism. These results are consistent with CO oxidation triggered by CO oxidative coupling with interfacial OH groups at Fe^{3+}-OH-Pt that also creates coordinatively unsaturated Fe sites for O_2 activation.

In terms of Pt use, the core-shell overgrowth structure described above is not an ideal structure because most Pt atoms are not located on the surface (Fig. 4A) (*1*, *27*). To maximize Pt use and Fe/Ni-OH-Pt interfaces as well, we developed an alloy-assisted strategy to maximize the use of Pt. In this strategy, ternary alloy PtFeNi NCs were prepared by thermally reducing metal precursors [i.e., $Pt(acac)_2$, $Fe(acac)_3$, and $Ni(acac)_2$] under 1 atm CO atmosphere and then aged in the air for 3 days to yield the highly active catalyst (denoted as PtFeNi) (Fig. 4A). The mean diameter of the PtFeNi NPs was 4.9 ± 0.5 nm. When the thermal reduction time at 513 K was 30 min, STEM analyses revealed that the PtFeNi NPs were mainly core-shell structures with Pt-enriched cores (Fig. 4, B and C, and fig. S28). However, Pt-enriched cores were not present in the PtFeNi NPs when the thermal reduction time at 513 K was extended to 1 hour (fig. S29). Each individual NP apparently had a single-crystalline face-centered cubic structure. However, more careful STEM-EDS investigations revealed an interwoven, highly irregular structure to the surface of the air-aged PtFeNi NPs (Fig. 4D and fig. S30) that improved the Pt use compared with those from both Pt NCs and Pt/$Fe(OH)_x$ or Pt/$FeNi(OH)_x$ NPs with the core-shell overgrowth structure.

As characterized by elemental mapping (Fig. 4E), the PtFeNi NPs exhibited compositional heterogeneities in the form of small interwoven domains (less than 3.5 Å) on their surfaces. The LEISS spectra (fig. S31) confirmed that Pt, Fe, and Ni were all exposed on the outermost surface. Both XANES and XPS spectra confirmed the presence of Fe^{3+} and Ni^{2+} oxidation states. EXAFS analyses (fig. S32) revealed that Fe and Ni in the PtFeNi catalyst were both six-coordinate with respect to oxygen, with average Fe-O and Ni-O bond distances of 1.99 ± 0.01 and 2.04 ± 0.01 Å, respectively (table S4). The O1s XPS spectrum indicated an OH:O ratio of 13 (fig. S33). These EXAFS and XPS studies demonstrated that PtFeNi NPs possessed the same interfacial sites discussed above for the Pt/$FeNi(OH)_x$ catalyst, which were active and stable for CO oxidation. As suggested by the temperature-programmed desorption measurements (fig. S34), besides the catalytically active sites that readily reacted with CO to yield CO_2, no further CO chemical adsorption sites were available on the surface of the PtFeNi catalyst. CO titration was thus used to determine the percentage of catalytic sites over the total Pt sites in the catalyst. As illustrated in table S5 (*20*), the numbers of catalytic sites depended on the composition and also the thermal reduction conditions of the NPs. The PtFeNi catalysts with high percentages of Pt-OH-M sites (up to 54% over the total Pt atoms) were readily prepared by extending the thermal reduction time at 513 K. The high percentage of catalytic sites is also supported by the rough NP surfaces with highly dispersed Pt, and the high coordination number (up to 1.6) of O on Pt (table S4) that would allow surface Pt atoms to form more than one Pt-OH-M active center. As compared to the overgrown Pt/$FeNi(OH)_x$ catalyst with the same amount of Pt, the catalytic performance of TiO_2-supported PtFeNi NPs (fig. S35) for CO oxidation was indeed enhanced by a factor of 1.4 to 1.8 (fig. S36). The PtFeNi catalyst exhibited the highest activity with a Fe/Ni molar ratio of ~0.5 (fig. S37). The PtFeNi catalyst exhibited very high stability, both in the reaction stream and during prolonged storage. No decay in the activity of the catalyst was experienced after more than 1 month in the reaction stream of CO with humid air (fig. S38).

The enhanced catalysis of the PtFeNi NPs over pure Pt NCs was also observed when γ-Al_2O_3 was used as the support (fig. S39). Even after being stored at room temperature in ambient air for 2 years, no deterioration of catalytic performance was found for the PtFeNi catalyst prepared by the alloy-assisted strategy. The excellent catalytic performance of the PtFeNi catalyst makes it a promising candidate for applications to remove CO in

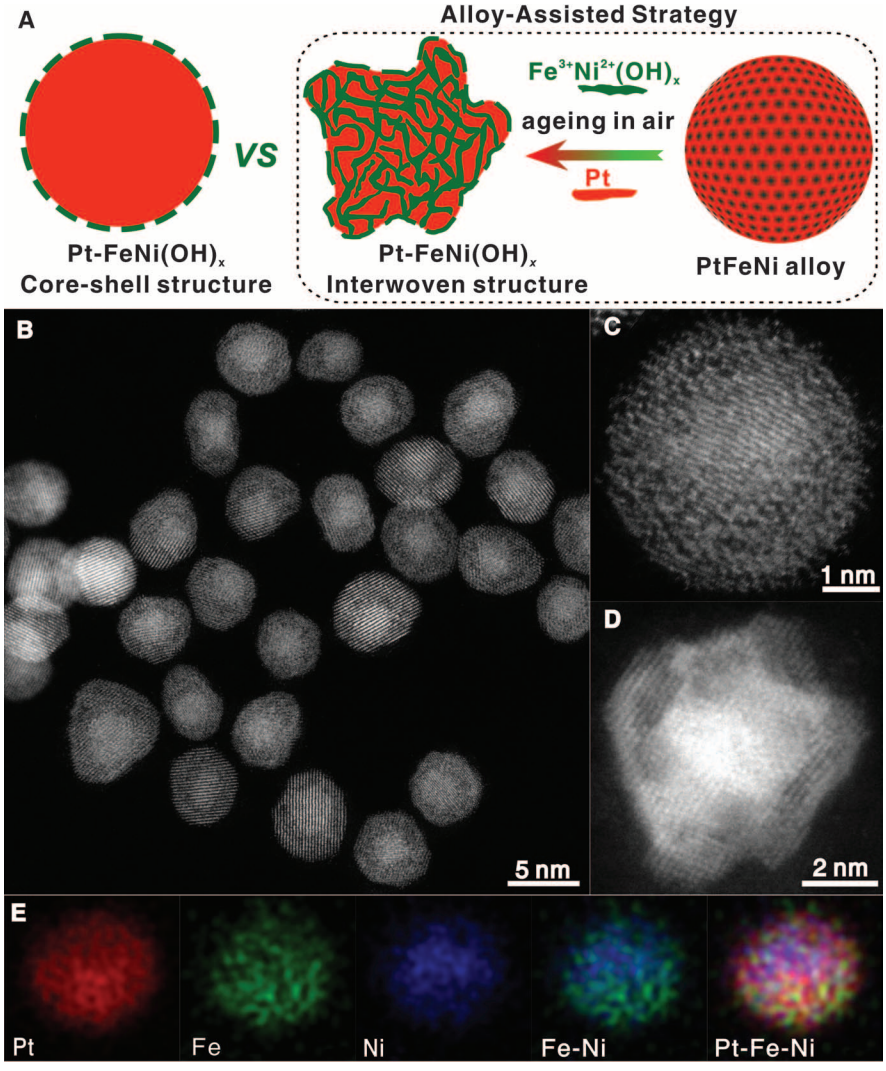

Fig. 4. Synthetic strategy, characterizations, and catalysis of a practical PtFeNi catalyst. (**A**) Cartoon showing the structural difference between the core-shell overgrowth Pt/$FeNi(OH)_x$ catalyst and the interwoven PtFeNi catalyst, and the alloy-assisted strategy for the synthesis of the PtFeNi catalyst. (**B**) Representative HAADF-STEM image of PtFeNi NPs. (**C** and **D**) High-resolution HAADF-STEM image of PtFeNi NPs before (C) and after (D) aging in air, respectively. (**E**) STEM-EDS elemental mapping of a single PtFeNi NP.

humid air or H_2-rich stream and trace H_2 in air (figs. S40 and S41). Creating submonolayer metal hydroxides on noble metal NCs is expected to provide an effective method to prepare efficient noble metal nanocatalysts for oxidative catalysis.

References and Notes

1. Q. Fu *et al.*, *Science* **328**, 1141–1144 (2010).
2. B. Qiao *et al.*, *Nat. Chem.* **3**, 634–641 (2011).
3. I. X. Green, W. Tang, M. Neurock, J. T. Yates Jr., *Science* **333**, 736–739 (2011).
4. M. S. Chen, D. W. Goodman, *Science* **306**, 252–255 (2004).
5. J. B. Park *et al.*, *Proc. Natl. Acad. Sci. U.S.A.* **106**, 4975–4980 (2009).
6. J. A. Rodriguez *et al.*, *Science* **318**, 1757–1760 (2007).
7. Q. Fu, H. Saltsburg, M. Flytzani-Stephanopoulos, *Science* **301**, 935–938 (2003).
8. Y. Yamada *et al.*, *Nat. Chem.* **3**, 372–376 (2011).
9. M. Cargnello *et al.*, *Science* **337**, 713–717 (2012).
10. R. Subbaraman *et al.*, *Nat. Mater.* **11**, 550–557 (2012).
11. R. Subbaraman *et al.*, *Science* **334**, 1256–1260 (2011).
12. V. R. Stamenkovic *et al.*, *Nat. Mater.* **6**, 241–247 (2007).
13. J. Zhang, K. Sasaki, E. Sutter, R. R. Adzic, *Science* **315**, 220–222 (2007).
14. G. W. Huber, J. W. Shabaker, J. A. Dumesic, *Science* **300**, 2075–2077 (2003).
15. H. Zhang, T. Watanabe, M. Okumura, M. Haruta, N. Toshima, *Nat. Mater.* **11**, 49–52 (2012).
16. B. H. Wu, N. F. Zheng, *Nano Today* **8**, 168–197 (2013).
17. G. A. Somorjai, A. M. Contreras, M. Montano, R. M. Rioux, *Proc. Natl. Acad. Sci. U.S.A.* **103**, 10577–10583 (2006).
18. T. S. Ahmadi, Z. L. Wang, T. C. Green, A. Henglein, M. A. El-Sayed, *Science* **272**, 1924–1926 (1996).
19. M. Cargnello *et al.*, *Science* **341**, 771–773 (2013).
20. See supplementary materials on *Science* Online.
21. B. J. Tan, K. J. Klabunde, P. M. A. Sherwood, *Chem. Mater.* **2**, 186–191 (1990).
22. T. E. Westre *et al.*, *J. Am. Chem. Soc.* **119**, 6297–6314 (1997).
23. M. Gong *et al.*, *J. Am. Chem. Soc.* **135**, 8452–8455 (2013).
24. Y. Han *et al.*, *Chem. Mater.* **20**, 360–363 (2008).
25. M. A. Henderson, *Surf. Sci. Rep.* **46**, 1–308 (2002).
26. L. R. Merte *et al.*, *Science* **336**, 889–893 (2012).
27. Q. Fu, F. Yang, X. Bao, *Acc. Chem. Res.* **46**, 1692–1701 (2013).

Acknowledgments: We appreciate the financial support from the Ministry of Science and Technology of China (2011CB932403) and the National Nature Science Foundation of China (21131005, 20925103, 21373167, 21033006, and 21333008). P.Z. appreciates the funding from Natural Sciences and Engineering Research Council of Canada. We also thank L. S. Zheng, Z. Q. Tian, X. Lu, Y. Wang, and S. C. Lin for helpful discussions, and Shanghai Supercomputer Center (SSC) for providing computational resources. X-ray absorption spectroscopy studies were carried out at the beamline 17C1 of the National Synchrotron Radiation Research Center (NSRRC) in Taiwan.

Supplementary Materials

www.sciencemag.org/content/344/6183/495/suppl/DC1
Materials and Methods
Figs. S1 to S41
Tables S1 to S5
References (*28*–*40*)

24 February 2014; accepted 9 April 2014
10.1126/science.1252553

Manipulation of Discrete Nanostructures by Selective Modulation of Noncovalent Forces

Takahiro Fukino,[1] Hyunho Joo,[1] Yuki Hisada,[1] Maiko Obana,[1] Hiroshi Yamagishi,[1] Takaaki Hikima,[2] Masaki Takata,[2] Norifumi Fujita,[1] Takuzo Aida[1,3]*

Covalent organic synthesis commonly uses the strategy of selective bond cleavage and formation. If a similar approach can be applied stepwisely to noncovalent synthesis, more exotic or challenging nanostructures might become achievable. Here, we report that ferrocene-based tetratopic pyridyl ligands, which can dynamically change their geometry by means of thermal rotation of their cyclopentadienyl rings in solution, assemble with $AgBF_4$ into discrete metal-organic nanotubes with large and uniform diameters. The nanotubes can be cut into metal-organic nanorings through selective attenuation of the inter-nanoring interaction via ferrocene oxidation. The resultant nanorings can be transferred onto inorganic substrates electrostatically or allowed to reassemble to form the original nanotube by the reductive neutralization of their oxidized ferrocene units.

In covalent organic synthesis, bond cleavage and formation are commonly used for the construction of complicated molecular structures. However, for noncovalent architectures, manipulation of the assembled structure is difficult because selective in situ attenuation and/or enhancement of noncovalent forces is hard to achieve. Although a variety of beautiful nanostructures have been noncovalently synthesized (*1*–*6*), even more exotic or hardly accessible self-assembled motifs might become available if there were methods to cut, paste, or merge assembled structures. With stepwise noncovalent synthesis, several exotic nanostructures were recently synthesized by using inorganic clusters (*7*, *8*), block copolymers (*9*–*12*), and small organic molecules (*13*) as assembling components, and some of those nanostructures were indeed shown to break up into thermodynamically inaccessible, low-symmetry pieces (*14*, *15*). However, such selective cutting requires prior stabilization of parent nanostructures by means of partial cross-linking, so that cut pieces are covalently linked.

We report the noncovalent synthesis of a large-diameter metal-organic nanotube, which can be preferentially "cut" into its constituent nanorings with a metal-organic structure. A key for the success in cutting the nanotube was the redox-active ferrocene motif used for our metal-ligating units $\mathbf{FcL_1}$ and $\mathbf{FcL_2}$ (Fig. 1A and figs. S1 to S4). Ligands $\mathbf{FcL_1}$ and $\mathbf{FcL_2}$, derived from 1,1′-bis(4-bromophenyl)-3,3′-bis(4-iodophenyl)ferrocene (*16*), carry a metal-coordinating 4-pyridyl group at each terminus of the four aromatic arms. Hence, they are tetratopic ligands. The triethylene glycol (TEG) side chains are for enhanced solubility of the ligands and better dispersibilities of assembled products in common organic solvents. Because ferrocene derivatives thermally rotate their cyclopentadienyl rings freely in solution (*17*), both ligands have the possibility of changing their tetratopic geometry dynamically (Fig. 1B, top). This "geometrical uncertainty" might give rise to the formation of ill-defined metal-organic structures but might also allow for more scope for modifying the assembled structures. As a metal ion source, we chose $AgBF_4$ (Fig. 1C) because its coordination chemistry with pyridine (Py) derivatives, forming a linear Py(N)–Ag(I)–(N)Py array, has been well established (*18*–*21*). If the ligand adopts an entropically favored noneclipsed geometry in solution, a sheet-like two-dimensional (2D) structure (Fig. 1B, bottom left) would result, in which the ligands are connected together by single Py(N)–Ag(I)–(N)Py bonds. On the other hand, if the ligand adopts an eclipsed geometry, the formation of a doubly bridged coordination polymer (Fig. 1B, bottom center) is expected. The doubly bridged connection should be more stable than the singly bridged one because of its multivalency and can also take an enthalpic gain as a consequence of possible π-stacking and Ag(I)–Ag(I) metallophilic interactions (Fig. 1D) (*18*–*20*). Although linear coordination polymers might be able to cyclize (Fig. 1B, bottom right), such a cyclization event, in general, is entropically disfavored.

Rather than any of the three anticipated products, the assembly of $AgBF_4$ with $\mathbf{FcL_1}$ yielded large-diameter nanotube $\mathbf{FcNT_1}$ (Fig. 1, C and E). As a typical example, an acetonitrile (MeCN) solution of a mixture of $\mathbf{FcL_1}$ (2.0 mM) and two equivalents of $AgBF_4$ (figs. S6, S7, S9, and S11) was allowed to stand at 25°C without stirring. After 4 hours, an aliquot of the reaction mixture was diluted with water, and the resultant suspension, negatively stained with uranyl acetate, was air-dried and then subjected to transmission electron microscopy (TEM). As shown in Fig. 2A, hollow cylinders ($\mathbf{FcNT_1}$) with a uniform "wall center–to–wall center" distance (nanotube diameter)

[1]Department of Chemistry and Biotechnology, School of Engineering, The University of Tokyo, 7-3-1 Hongo, Bunkyo-ku, Tokyo 113-8656, Japan. [2]RIKEN SPring-8 Center, 1-1-1 Kouto, Sayo, Hyogo 679-5198, Japan. [3]RIKEN Center for Emergent Matter Science, 2-1 Hirosawa, Wako, Saitama 351-0198, Japan.

*Corresponding author. E-mail: aida@macro.t.u-tokyo.ac.jp